AIMS Materials Science, 12(3): 621–648.
DOI: 10.3934/matersci.2025027
Received: 17 May 2025
Revised: 04 July 2025
Accepted: 07 July 2025
Published: 16 July 2025

http://www.aimspress.com/journal/Materials

Research article

Finite element modelling and experimental validation of laser transmission welding of oak wood fiber reinforced polypropylene composite

Munyaradzi Kapuyanyika*, Albert Uchenna Ude and Vivekanandhan Chinnasamy

Department of Mechanical, Industrial and Energy Engineering, Botswana International University of Science and Technology, P. Bag 16, Palapye, Botswana

* **Correspondence**: Email: munyabk@gmail.com; Tel: +267-72-510-267.

Abstract: Finite element analysis (FEA) was performed to determine the weld width in laser transmission welding for three different configurations. The first configuration involved joining a 100% pure polypropylene transparent part to an absorbent part doped with 0.2 wt% carbon black, without fiber reinforcement. The second configuration incorporated 15 wt% natural fiber into the absorbent part, while the third configuration incorporated 15 wt% natural fiber into the transparent part. The FEA employed a 3D subroutine heat source accounting for thermal convection, conduction, and radiation, run within the ABAQUS software. Material properties were obtained through various methods. Thermogravimetric analysis (TGA) and differential scanning calorimetry (DSC) were used to assess thermal stability and specific heat capacity. Optical properties, including transmittance, reflectance, and absorbance, were measured experimentally using near-infrared spectroscopy and integrated into the model. The effective thermal conductivity of fiber-reinforced polypropylene was calculated using homogenization of a representative volume element (RVE) in ABAQUS, while density was determined using the rule of mixtures (ROM). Upon completion of the simulations, the predicted weld widths were compared with the experimental results.

Keywords: effective thermal conductivity; homogenization; laser transmission welding; finite analysis; thermal modeling; rule of mixtures

1. Introduction

Natural fiber-reinforced polymers, such as polypropylene reinforced with oak wood fiber, are gaining popularity due to their environmental advantages and increased sustainability [1]. Nevertheless, because natural fibers greatly affect optical and thermal characteristics, understanding their behavior during laser transmission welding remains a challenge. Characterizing the optical and thermal properties of such composites experimentally and incorporating them into a simulation are crucial for effective modeling of the laser transmission welding (LTW) process. This study fills this gap by combining finite element modeling with experimental characterization, including optical transmittance, reflectance, absorbance, and thermal stability. Homogenization methods based on the representative volume element (RVE) were used to determine the fiber-reinforced polypropylene's effective thermal conductivity. In an effort to improve the accuracy of the simulation of the laser–material interactions, optical characteristics were evaluated experimentally and incorporated into the model.

Finite element analysis (FEA) has gained recent attention and is now indispensable to engineering analysis and design. In most engineering branches, FEA is now used to reduce the cost incurred in conducting experiments by analyzing the behavior of components under different conditions and predicting the properties of uncommon composite materials [2]. Most researchers in laser transmission welding (LTW) have extensively utilized FEA to predict attributes such as transient temperature distribution, weld seam shape, and thermally induced stress [3–6]. Additionally, during the LTW process, phase changes such as melting, decomposition, and solidification are simulated using the FEM, which enables the determination of weld seam shape and porosity caused by overheating of the thermoplastics during LTW [7]. Heat conduction, convection, and radiation equations determine the transient temperature distribution within the volume of the material by calculating the phase fraction at every element of the meshed area of interest, enabling mechanical analysis to determine strain and stresses in the material. When conducting a transient heat transfer simulation for LTW, the density of the material being joined is essential. When dealing with composite materials, such as natural fiber-reinforced polymers, the material properties of the composite are often predicted using models like the rule of mixtures (ROM), which enables the estimation of key parameters, including density and stiffness, based on the contribution of the individual constituents. Deng et al. [8] successfully applied ROM to determine Young's modulus and tensile strength of unidirectional fiber reinforced polymers. Nguyen et al. [9] predicted the tensile strength of longitudinal printed high-impact polystyrene samples, which were fabricated via fused filament fabrication. Yerbolat et al. [10] used the rule of mixture based on a Monte Carlo simulation to accurately determine Young's modulus of composite materials.

When it comes to the LTW of materials, the transparency of the material to the specific incident laser beam is essential because it affects the laser intensity that reaches the absorbent part. Therefore, in FEA, estimating optical properties is critical. Ray tracing is the most common optical method for simulating radiative transfer in infrared LTW problems [1]. The infrared laser beam diverges microscopically due to interactions between the matrix fiber and fibers in composite materials within the transparent part of the LTW process. As a result, modeling the propagation of the laser beam in heterogeneous transparent media is critical. The ray tracing model has been used to estimate the laser beam intensity that reaches the weld interface in LTW [11]. Xu et al. [12] utilized 3D transient model analysis to determine that heat conduction dominates over convection and that the interface temperature is critical for the molten formation and weld size during LTW of polyethylene

terephthalate (PET) and stainless steel. Wang et al. [13] Developed a new finite element model for the low-temperature warping of thermoplastics, which considers thermal contact conductance. Jabeen et al. [1] used 3D numerical modeling and ray tracing simulation to determine the effect of fiber orientation on laser beam scattering and the consequent impact of the beam reaching the weld interface. Chen et al. [14] developed a 3D thermal model to determine the temperature field distribution and weld geometry for the LTW of transparent polymethyl methacrylate (PMMA) using multi-core copper wire. Acherjee et al. [15] developed a finite element analysis and designed experiments for modeling contour LTW of polycarbonate materials. Ali et al. [16] used finite element analysis simulation to investigate the effect of carbon black concentration on high-speed laser transmission welding and its consequent impact on material degradation. AnhDuc et al. [17] developed a 3D thermal model to validate the effect of light scattering on the temperature interface during LTW of 3D-printed thermoplastics. Acherjee et al. [18] developed a 3D finite element model considering the effect of heat conduction, convection, radiation, and dilution in the LTW of polycarbonate and acrylonitrile butadiene styrene (ABS). Long et al. [19] integrated a finite element model and thermogravimetric analysis to predict thermal degradation during the LTW of PMMA. Kumar et al. [20] determined the effect of beam wobbling on the LTW of acrylic and polycarbonate using an experimental study, mathematical modeling, and process optimization. Xu et al. [12] used finite volume-based simulation to predict molten pool behavior during LTW of PET and SUS304 stainless steel alloy.

In another research, the authors experimentally determined the optical properties of the materials to be joined using LTW. Also, to understand the thermal performance of uncommon composite materials, modeling the effective thermal conductivity can be done using numerical modeling [21]. Some common boundary conditions used in modeling effective thermal conductivity include mixed boundary conditions and uniform temperature gradients [21]. In this paper, we calculate the effective thermal conductivity of the composite material to be subjected to LTW. The calculated effective thermal conductivity is then utilized as the thermal conductivity property of the composite material in the FEA of the LTW of the polypropylene composite materials. To understand the effect of natural fibers on the LTW of polypropylene in the first setup, both the absorbent part and the transparent part are not reinforced. In the second setup, the transparent part is not reinforced, while the absorbent part is reinforced with 15 wt% oak wood fiber. In the third instance, the transparent part is reinforced with 15 wt% oak wood fiber, while the absorbent part is not. Upon completion of the simulation process, the simulated weld width results are compared to the experimentally determined weld width. Other properties of the composite material vital to conducting FEA of LTW are determined experimentally, and others such as density, specific heat capacity, transmittance, absorptivity, and reflectivity are obtained from open literature.

2. Materials and methods

Homopolypropylene granules were supplied by Shanghai Qishen Plastic Industries. Shijiazhuang Yuancang Trading supplied the carbon black, and Guangdong Yaunfang Technology supplied the oak wood powder for the fabrication of samples to be considered in this study. Four different samples were fabricated using injection molding. The first material consisted of 100% polypropylene (PP); the second was composed of polypropylene [containing 0.2% carbon black (CB) by weight of the matrix material]; the third consisted of polypropylene (containing 0.2% carbon black and 15% oak wood powder by weight of the matrix material). The fourth material was composed of

polypropylene (containing 15% oak wood powder by weight of the matrix material). All are shown in Figure 1. The PP, CB, and oak wood powder were mixed at the required ratios using a twin extruder at an extrusion speed of 200 rpm and an extrusion temperature of 190 ℃. These granules were then injected using a plastic injection molding machine to form 140 × 220 × 4 mm samples at an injection speed of 0.230 m/s and injection pressure of 210 MPa, which were then cut to the required sizes of 70 × 35 × 4 mm. In this study, SAT 130/30 twin screw extruder and a Haitian 160T injection machine model were used to prepare the polypropylene plaques. A Leco thermogravimetric analyzer (TGA) 701 thermogravimetric analyzer and a Mettler Toledo DSC/TGA 3+, USA TGA(DSC) were used for the TGA experiments at a heating rate of 5 °C/min from room temperature to 600 ℃ under a nitrogen environment with a nitrogen flow of 20 mL/min for thermal analysis of the polypropylene materials. An Agilent 4500 NIR (Fourier transform near-infrared) spectrometer was used to measure the optical properties of the samples. A Micromeritics AccuPyc II 1340 gas pycnometer model was used to measure the density of oak wood powder, which was found to be 1.5 g/cm^3. For validation of the simulation results, a Ger-sonic plastic welding machine model GS-3DLPW-300-35, equipped with a diode semiconductor laser with a beam diameter of 1 mm using a wavelength of 976 nm, was used to conduct the LTW experiments. An Instron Tinius Olsen testing machine model H50KT was used to break the weld joints by applying tensile forces to the joined samples using a crosshead speed of 0.5 mm/min. A Nikon Eclipse E200 microscope with a minimum magnification of 10× and an accuracy of 0.005 μm was employed for microscopic imaging of the apparent weld seam width.

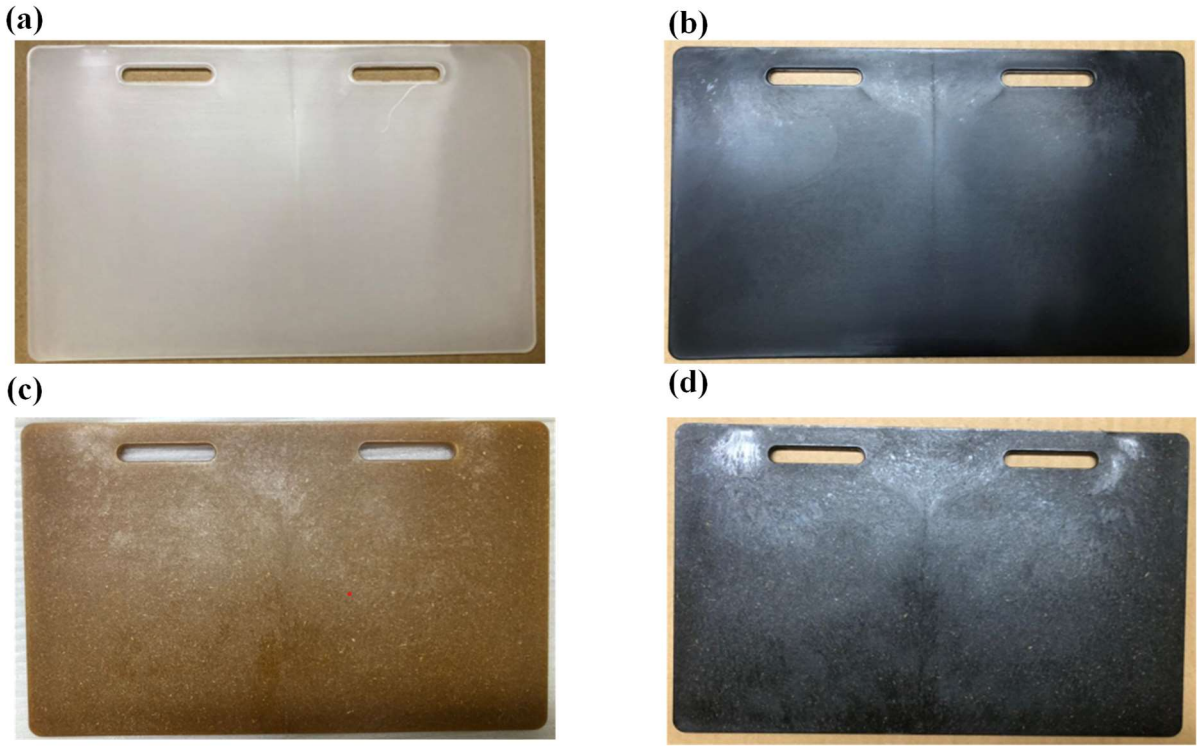

Figure 1. (a) 100% polypropylene; (b) polypropylene containing 0.2 wt% carbon black; (c) polypropylene containing 15 wt% oak wood fiber; (d) polypropylene containing 0.2 wt% carbon black and 15 wt% oak wood fibers.

2.1. Optical properties

The optical properties of the samples were measured using an Agilent 4500 NIR (Fourier transform near-infrared) spectrometer by passing a light of 987 nm wavelength through the samples, recording the amount of absorbed light. The transmittance was determined by assessing the amount of light that passes through compared to the initial light intensity. The measurements were taken for three random samples of each type of polypropylene plaque, and the average was taken as the final optical transmittance, reflectance, and extinction coefficient, also known as absorption coefficient reading, as shown in Tables 1 and 2, which were used for the simulation of the LTW process. Transmittance experiments were only taken for the materials to be used as transparent parts, and the extinction coefficient was only taken for the materials to be used as absorbent parts.

Table 1. Optical transmittance of polypropylene materials.

Material	Transmittance
100% Polypropylene	80%
Polypropylene containing 15% oak wood powder by weight of the matrix material	60%

Table 2. Reflectance and extinction coefficients of carbon black–doped polypropylene materials.

Material	Reflectance	Extinction coefficient (1/mm)
Polypropylene containing 0.2% carbon black by weight of the matrix material	0.23%	14
Polypropylene containing 0.2% carbon black and 15% oak wood powder by weight of the matrix material	0.11%	30

2.2. Particle size distribution of oak wood powder

The oak wood fibers used for reinforcing the PP were examined using field emission scanning electron microscopy (FESEM), model JSM-7100F. SEM images were analyzed with the help of Image J software to determine the particle size distribution of the oak wood powder, as shown in Figure 2, and the density of the oak wood powder was determined using a gas pycnometer, taking the average of five measurements.

For determining the density of the composite material, the rule of mixtures based on weight fractions was used as shown in Eq 1:

$$\frac{1}{\rho c} = \frac{\omega f}{\rho f} + \frac{\omega m}{\rho m} \tag{1}$$

where ρc, ωf, ωm, ρf, and m represent the density of the composite, the weight fraction of fiber, the weight fraction of matrix material, the density of fiber, and the density of matrix material, respectively. In this study, the composite material was composed of 15 wt% oak wood fiber and 85 wt% polypropylene, with a fiber density of 1509.8 kg/m^3 determined experimentally using a gas pycnometer. For the polypropylene, a density of 0.9 kg/m^3 was taken from literature [22]. Therefore, substituting these values into Eq 2 gives:

$$\frac{1}{\rho c} = \frac{0.15}{1509.8} + \frac{0.85}{900} = 0.0010388 \tag{2}$$

Therefore, the density of the composite material can be approximated as shown in Eq 3:

$$\rho c = \frac{1}{0.0010388} \approx \frac{962.6kg}{m^3} \tag{3}$$

The estimated value is used for assigning density for the transient heat transfer simulation.

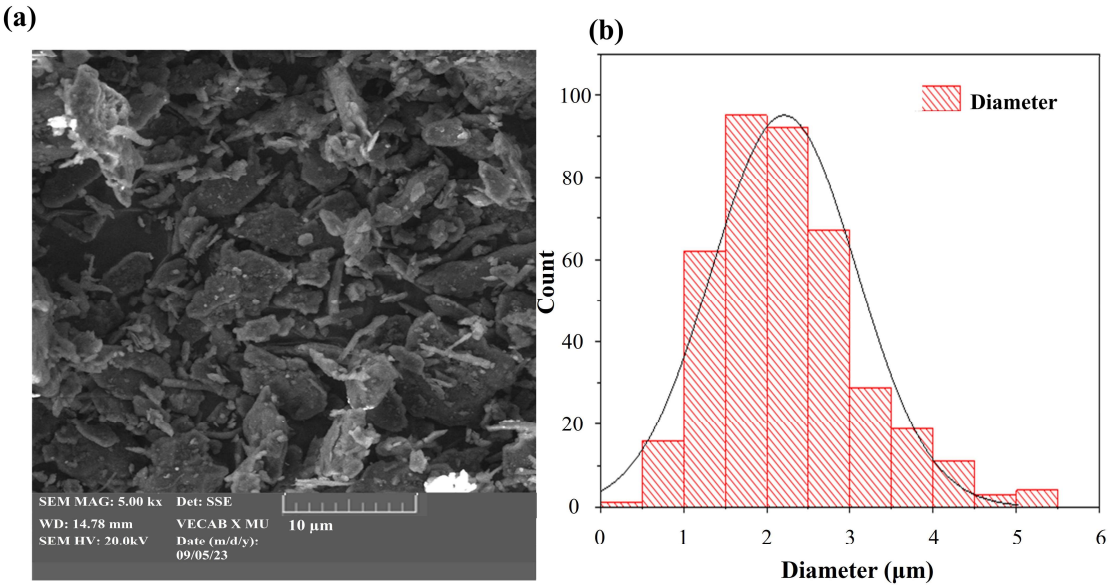

Figure 2. (a) Microscopic image of the oak wood fibers. (b) Oak wood fibers particle size distribution histogram.

2.3. Thermal characterization of polypropylene samples

Small specimens of approximately 10 mg of the TGA and TGA (DSC) were used in the TGA to determine the thermal stability and specific heat capacity of the fabricated samples. The thermogravimetric analysis was done in a nitrogen environment at a heating rate of 5 °C/min. The samples were heated from room temperature to 600 °C in a nitrogen flow of 20 mL/min. In this study, we used TGA (DSC) data to calculate the latent heat of fusion, determine the inset and offset temperature of the melting thermodynamic event, and calculate the temperature-dependent specific heat capacity. The latent heat of fusion was determined by dividing the heat flow by weight as shown in Eq 4. The result was used as the y-axis and plotted against time as the x-axis.

$$\frac{heat\ flow}{weight} = \frac{\frac{mJ}{s}}{mg} = \frac{J}{sg} \tag{4}$$

Finally, we calculated the dip area which is represented by Eq 5 using Origin software to determine the latent heat of fusion, as shown in Figure 3.

$$\frac{J}{sg} \times s = \frac{J}{g} \tag{5}$$

The unit of the integral area is J/g, which represents the enthalpy of fusion.

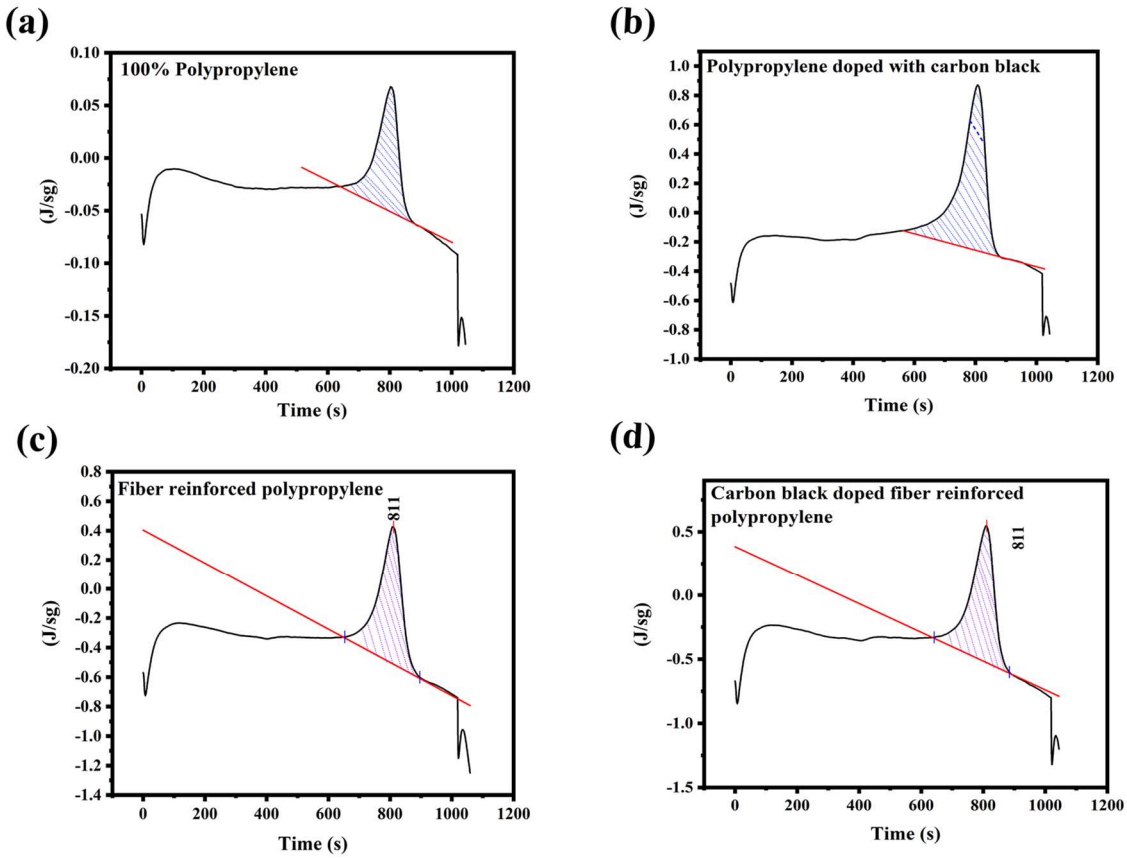

Figure 3. Heat flow per unit mass curves plotted as a function of time for (a) 100% polypropylene; (b) polypropylene containing 0.2 wt% carbon black; (c) polypropylene containing 15 wt% oak wood fiber; and (d) polypropylene containing 0.2 wt% carbon black and 15 wt% oak.

The TGA also provides essential data on the material's melting properties, including melting temperature, crystallization behavior, thermal stability, and decomposition temperature, which helps determine parameter limits to enhance welding quality. TGA and TGA (DSC) tests considered the four samples, which are 100% polypropylene, polypropylene containing 0.2% CB by weight of the polymer matrix, polypropylene containing 15% oak wood powder by weight of the polymer matrix, and polypropylene containing 0.2% CB and 15% oak wood powder by weight of the polymer matrix. Samples of about 10 mg were used in the TGA to undergo heating cycles from room temperature to 600 ℃ at a heating rate of 5 ℃/min and nitrogen flow of 20 mL/min. Figure 4 shows the weight loss curves for the samples during the heating cycle; the material was found to be stable for the temperature range of our interest, 160 to 200 ℃, where welding of PP samples occurs. From Figure 4, it can be seen that for 100% PP from low temperatures up to about 350 ℃, the curve shows a minimum weight loss of about 1.59%, showing that the material will be stable.

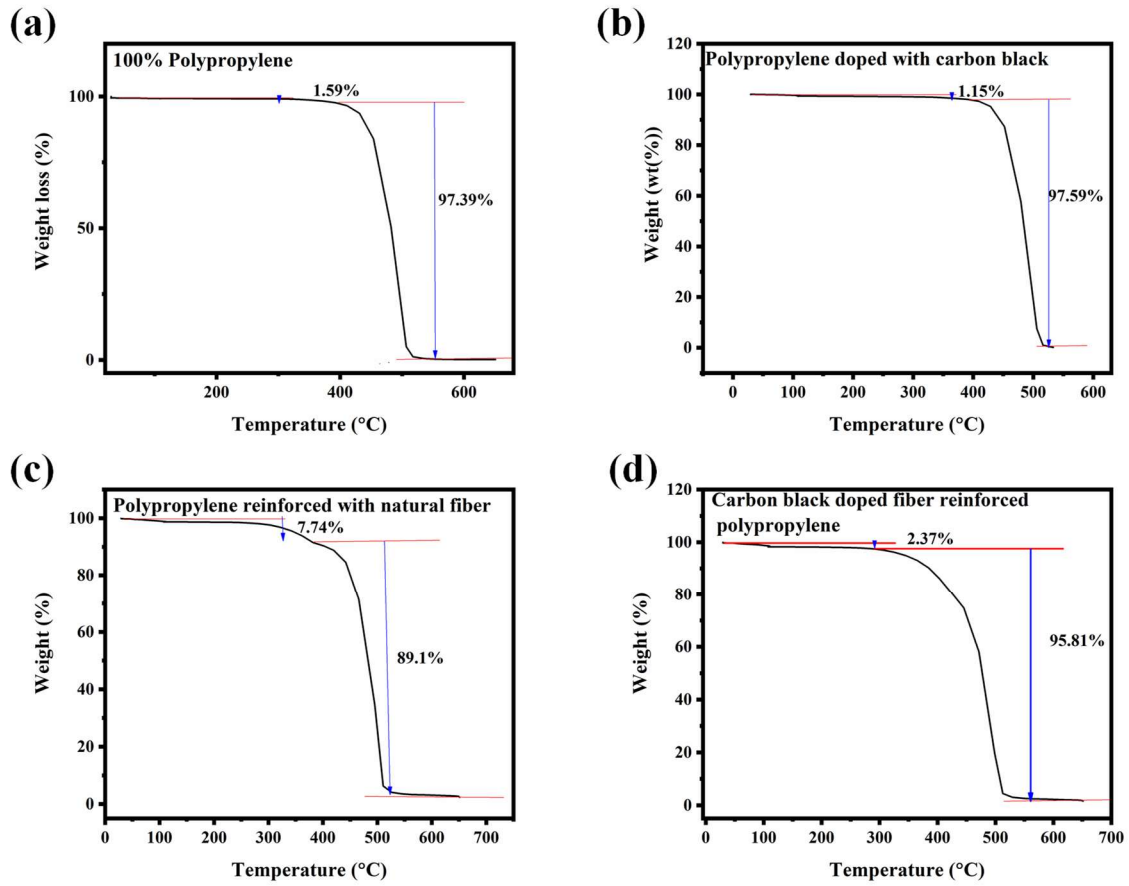

Figure 4. TGA curves for (a) 100% polypropylene; (b) polypropylene with 0.2 wt% carbon black; (c) polypropylene containing 15 wt% oak wood; and (d) polypropylene containing 15 wt% oak wood fiber and 0.2 wt% carbon black.

The slight loss in weight is due to low-molecular-weight components and volatiles. A significant weight loss of about 97.39% occurs from a temperature of 350–500 ℃, representing the primary decomposition of the sample. Hence, the material is thermally stable to approximately 350 ℃, which is above our target operating temperature for the LTW of PP. Figure 4 shows the thermal stability of PP doped with CB, indicating that from room temperature up to 400 ℃, PP has a minimum weight loss of about 1.15%, proving excellent stability of the material in this range. A significant weight loss of about 97.59% occurs in the temperature range of 400–500 ℃, showing material decomposition and degradation of the material structure. Figure 4a shows that carbon black enhances thermal stability at higher temperatures. Figure 4c shows the thermal stability of PP reinforced with 15 wt% oak wood powder. The samples show a minimum weight loss of about 7.74% from room temperature to about 250 ℃, evaporation of moisture, and decomposition of low-molecular-weight components. From 250 to 500 ℃, a significant weight loss of 89.1% occurs, showing primary thermal decomposition and degradation of the polymer matrix and fiber structure. Compared to Figure 4a, oak wood powder reduces the thermal stability of PP. Figure 4d shows the thermal stability of PP containing 0.2% CB and 15% oak wood powder by weight of the polymer matrix. The curve shows a minimal weight loss of about 2.37% from room temperature up to 300 ℃. This is due to the evaporation of moisture and low-molecular-weight volatiles. In this region, the material is stable.

From 300 to 600 ℃, a major thermal degradation occurs, shown by a significant weight loss of about 95.81%. When compared to Figure 4c, carbon black significantly improved the thermal stability of the oak wood fiber–reinforced polypropylene.

2.4. Specific heat capacity

For determining the specific heat capacity, we plot temperature on the x-axis; for the y-axis, we multiply the heat flow by time, divide by the weight, and then plot it on the y-axis, as shown in Eq 6.

$$y - axis = \frac{(heat\ flow)\times(time)}{(weight)\times(temperature} = \frac{J}{g℃} \tag{6}$$

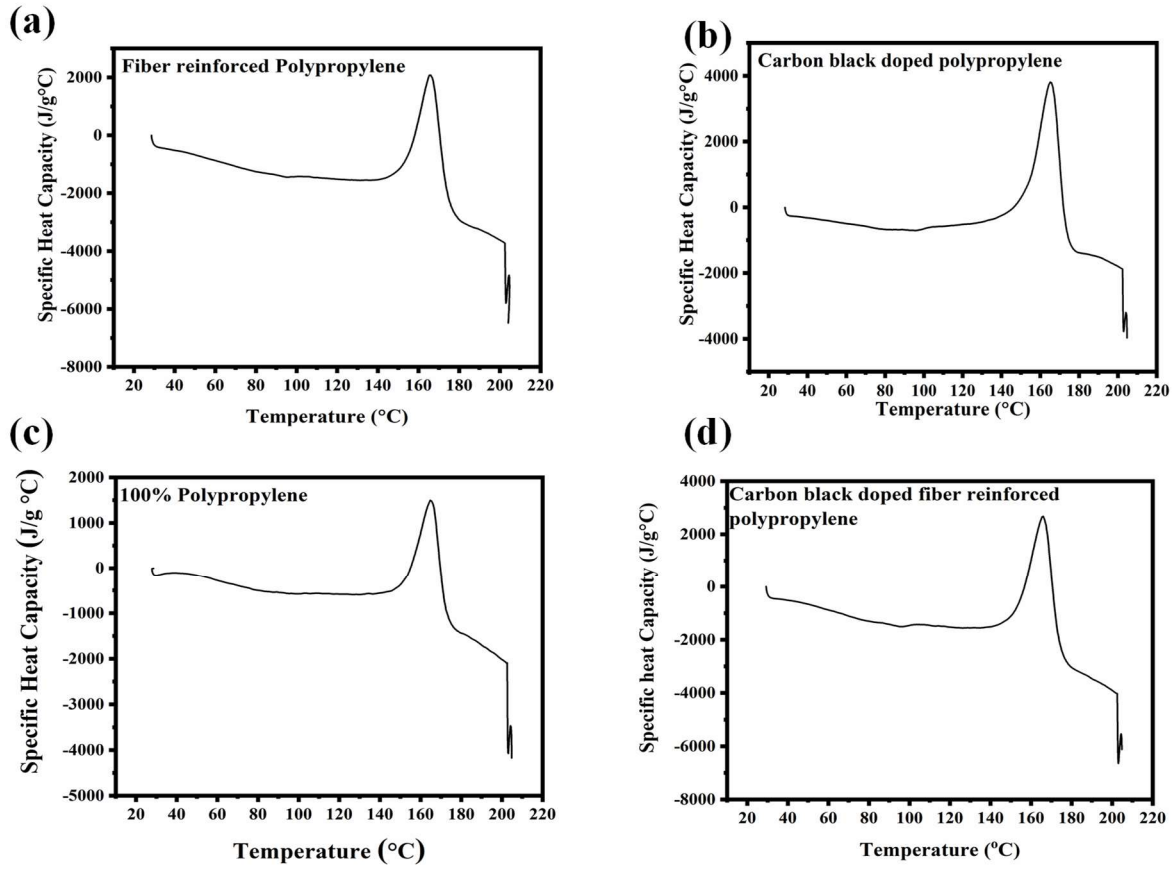

Figure 5. Temperature-dependent specific heat capacity for (a) 100% polypropylene; (b) polypropylene with 0.2 wt% carbon black; (c) polypropylene containing 15 wt% oak wood; and (d) polypropylene containing 15 wt% oak wood fiber and 0.2 wt% carbon black.

The units for the y-axis represent the units for the specific heat capacity. Therefore, the graphs in Figure 5 represent the specific heat capacity across a range of temperatures from the x-axis temperature values. We can, therefore, determine the initial melting temperature and the final temperature. From room temperature, the specific heat capacity values show little change as temperature increases to about 140 ℃. This indicates minimal thermal transitions. There is a sharp endothermic peak in the temperature range of 160–170 ℃. This peak represents the melting point of polypropylene. After 170 ℃,

the specific heat capacity decreases, corresponding to the completion of the melting process. The graph shows a sharp curve at about 200 ℃, which suggests the onset of thermal degradation of the material. The thermal behavior of the four graphs in Figure 5 is similar because the fundamental polymer matrix remains the same. Additives of carbon black and oak wood fiber slightly affect the heat capacity due to their thermal conductivity. However, they do not change the molecular structure of polypropylene; therefore, the melting and degradation of all samples occur at nearly the same temperatures.

2.5 Effective thermal conductivity numerical analysis using FEA

It is important to model the effective thermal conductivity to determine the thermal performance of the composite material to be used in LTW. In this study, we utilized a numerical model based on the finite element method to determine the effective thermal conductivity of oak wood fiber–reinforced polypropylene. Three different sizes of the cubic representative volume element (RVE), 80, 100, and 120 μm^3, and mixed boundary conditions were used for modeling. The fibers are randomly oriented, and they are assumed to be non-overlapping. The range of the fiber diameters was based on the particle size distribution of the oak wood fiber. The evaluation of the effective thermal conductivity of the heterogeneous media in this study depended on the assumption of an equivalent homogeneous medium. This study used the steady-state energy Eq 7 (Fourier law) in the RVE subject to thermal gradient LTW conditions.

$$\vec{\varphi} = -\lambda \overrightarrow{grad} T \tag{7}$$

Here, T and λ represent the material's temperature and thermal conductivity. The effective thermal conductivity of the heterogeneous material is then determined using the Fourier relation given in Eq 8. The temperature difference is applied between the 2 sides of the RVE, which is parallelepipedal.

$$K_{eff} = \frac{-LQ}{S|\Delta T|} \tag{8}$$

Where ΔT, L, Q, and S are the applied thermal gradient, the thickness of the sample, and the heat flux through the sample. Numerical simulation determines the average flux across the sample perpendicular to the surface where the temperatures are imposed. The following conditions should be applied to use Eq 8 effectively:

1. One-dimensional heat transfer is considered, and adiabatic conditions are applied to all boundaries parallel to the heat flow direction.
2. Linear variation in temperature is assumed to prevail throughout the material thickness.
3. The expression permits the estimation of the effective thermal conductivity in the temperature gradient direction, thereby doing the calculations in all three Cartesian directions.
4. The thermal contacts between the polymer matrix and the oak wood fibers are assumed to be in perfect contact without any thermal contact resistance between the two materials.

2.6. Numerical modeling

This study utilized ABAQUS finite element software to perform numerical modeling. In this work, we used a Python script to generate random fibers in 3D space. The fibers are then immersed in the

matrix material using ABAQUS GUI. From the Python script, it was possible to manipulate the fiber volume fraction, RVE dimensions, fiber length, and fiber radius. The fibers were modeled as circular cylinders, and it was possible to manipulate the range of randomly selected fiber diameters.

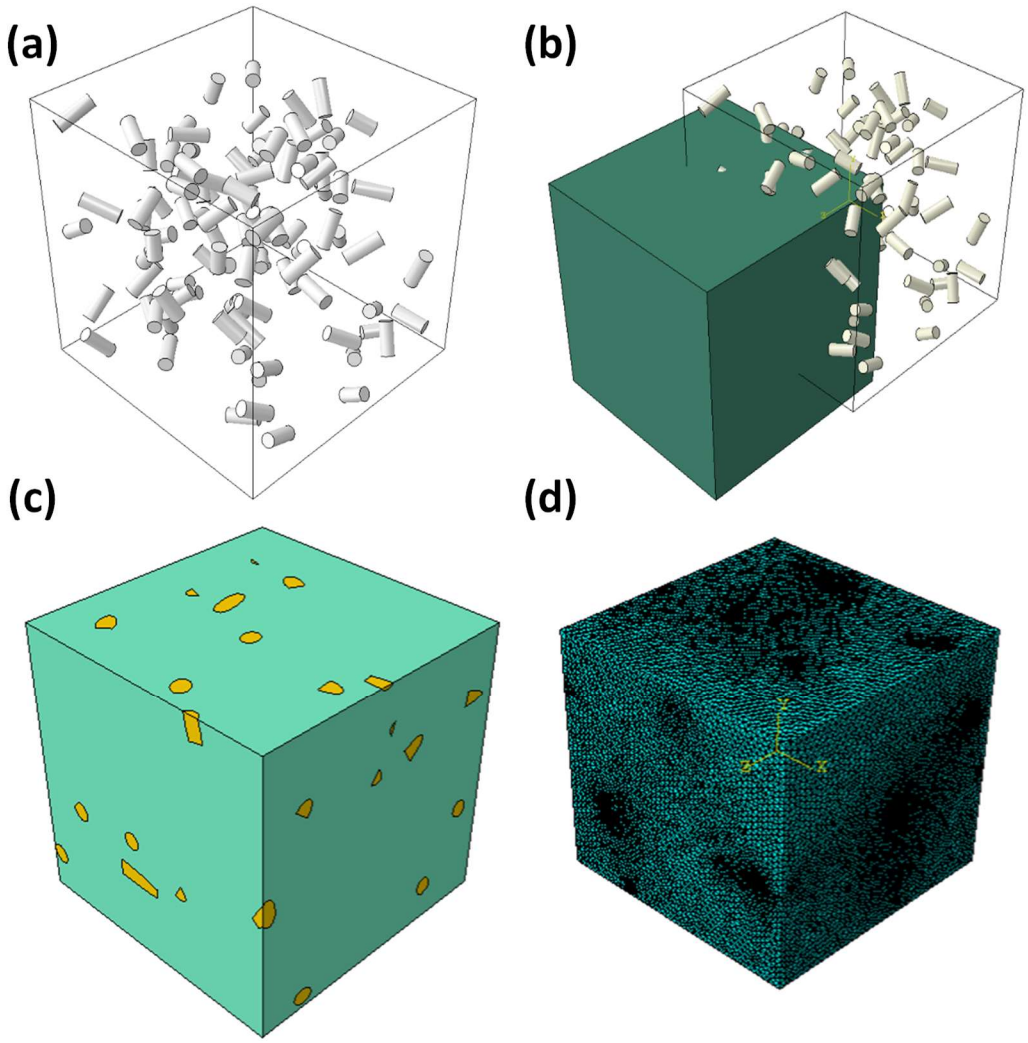

Figure 6. Schematic representation and modeling workflow of composite microstructure: (a) random fiber distribution; (b) assembly of matrix and fibers; (c) complete trimmed composite material; and (d) meshed composite representative volume element.

1. Before running the script, the volume fraction is defined as 15%, and the diameter of the fibers ranges from 1 to 5 μm based on the particle size distribution and a fiber length of 10 μm. After these fiber attributes were defined within the Python code, the Python script was run in Abaqus, and the fibers were randomly generated, as shown in Figure 6a.

2. Another part was modeled for the matrix material based on the RVE size of our choice, which was done for 3 RVE sizes (100, 120, and 80 μm^3), as shown in Figure 6b. The two materials were then assembled and trimmed the result RVE of the composite material is shown in Figure 6c.

3. In the third step, the material properties of the matrix material were assigned, and the thermal conductivity and density were based on the open literature [22]. For assigning the material properties of oak wood fiber, the thermal conductivity was taken from open literature, which was 2.0 W/(m·K) [23].

The density of the oak wood fiber was measured experimentally using a gas pycnometer, and it was found to be 1.5 g/cm^3.

4. This paper used steady-state heat transfer to define the step module.

5. For the interaction module, we applied the convection coefficient of heat transfer for polypropylene of 10 W/(m^2·K) [16] based on the literature review, and the sink temperature was defined as 25 ℃.

6. In the load module, a mixed boundary condition was imposed on the model following the mixed boundary conditions, with one hot side set at a temperature of 280 ℃ and the rest of the surfaces set at room temperature, which was 25 ℃.

7. A meshing tool in Abaqus is used to generate the finite elements of the composite material model. The finite element type used in this study was the quadratic tetrahedron (DC3D10), and the element size was verified to ensure it did not affect the results, as shown in Figure 6d.

8. The composite material model is then complete and ready for steady-state heat simulation, which was done in the job module.

This paper used mixed boundary conditions to compute the effective thermal conductivity in three dimensions based on Eq 9. In the mixed boundary condition, we imposed the hot temperature on one side and the cold temperature on the opposite side, as illustrated by Eq 10. The remaining four sides of the RVE are considered to be adiabatic, illustrated using Eq 11 within the Abaqus software.

$$\frac{\partial}{\partial x}\left(k_{x,y,z}\frac{\partial T}{\partial x}\right)+\frac{\partial}{\partial y}\left(k_{x,y,z}\frac{\partial T}{\partial y}\right)+\frac{\partial}{\partial z}\left(k_{x,y,z}\frac{\partial T}{\partial z}\right)=0 \tag{9}$$

$$T|_{z=0}=T_{cold};T|_{z=z}=T_{hot} \tag{10}$$

$$\left.\frac{\partial T}{\partial x}\right|_{x=0}=\left.\frac{\partial T}{\partial x}\right|_{x=X}=0;\left.\frac{\partial T}{\partial y}\right|_{y=0}=\left.\frac{\partial T}{\partial y}\right|_{y=Y}=0 \tag{11}$$

The modeling was done for three different RVE sizes: 80, 100, and 120 μm^3.

2.7. Estimation of the effective thermal conductivity from the FEM computation

The FEM simulation was conducted using mixed boundary conditions, which can be evaluated for the homogeneous effective conductivity of the composite material. The conduction heat flux density can be accessed in the ABAQUS software at every nodal point across the RVE, known as the reaction flux, and is abbreviated as RFL11 within the ABAQUS software. Eq 12 is utilized to determine the effective thermal conductivity.

$$k_{eff}=\frac{|\sum RFL11|.\boldsymbol{e}}{\boldsymbol{S}.\boldsymbol{\Delta T}} \tag{12}$$

Where S, ΔT, e, and $\sum RFL11$ represent sections of the faces, the temperature difference between the two faces, the thickness of the REV in accordance with the temperature gradient, and the total heat flux density crossing the REV from hot to cold faces. The effective thermal conductivity was determined for the RVE as shown in Figure 7.

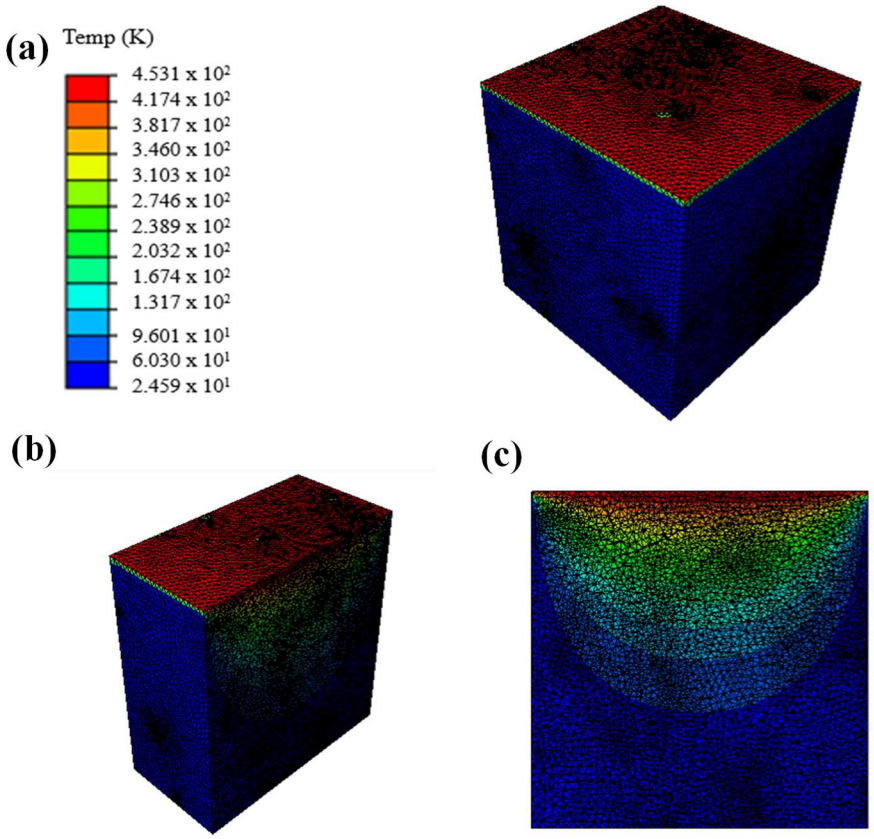

Figure 7. Heat profile of the steady-state heat transfer modeling using mixed boundary conditions of (a) the 3D complete model; (b) and (c) the cross-sectional heat profiles.

The results obtained for the thermal conductivity, shown in Table 3 were then utilized to assign material properties of the composite materials as homogeneous materials in the simulation of the LTW of the same materials.

Table 3. Determined effective thermal conductivity for different RVE sizes.

RVE size (μm^3)	Determined effective thermal conductivity (W/mK)
80	0.207
100	0.211
120	0.209

Other material properties for polypropylene were determined from open literature and utilized for assigning properties for polypropylene and oak wood fibers, as shown in Table 4.

Table 4. Temperature-dependent material properties.

Material	Property	Temperature-dependent data
Polypropylene [22]	Density ρ (g/m^3)	0.9
	Thermal conductivity k (w/m^{-1}k^{-1})	k = (1.866 × 10^{-4})T + 0.188, for 20 °C ≤ T ≤ 150 °C k = –(8.02 × 10^{-5})T + 0.234, for T > 150 °C
	Specific heat Cp (kJkg^{-1}k^{-1})	Cp = (3 × 10^{-3})T + 1.840, for 20 °C ≤ T ≤ 150 °C Cp = (1.4 × 10^{-3})T + 2.08, for T > 150 °C
Oakwood [23]	Thermal conductivity k (W/m^{-1}k^{-1})	0.2

2.8. Finite element modeling of laser transmission welding

This study uses ABAQUS software to model contour LTW for modeling the samples in a lap joint configuration. The transient 3D heat transfer model was developed to predict the weld width at the surface interface of the samples. Three sets of samples are considered. The first sample consists of 100% PP as the transparent part and PP doped with 0.2% CB as the absorbent part. The second set consists of 100% PP as the transparent part and an absorbent part comprising PP containing 0.2% CB and 15% oak wood fiber in the matrix material. For the third set of samples, the transparent part was composed of PP containing 15% oak wood fiber by weight to matrix material, and the absorbent part was composed of PP containing 0.2% CB by weight to matrix material. The assumptions made in this study are that the fiber-reinforced samples are homogenous, the laser beam had a Gaussian laser intensity distribution, there is perfect contact between the transparent and the absorbent part, and the polypropylene samples exhibited isotropic thermal properties.

2.9. Transient heat transfer model

The heat conduction mechanism is expressed in Eq 13 and is used to generate the transient temperature field during the contour laser transmission welding.

$$\rho c\left(\frac{\delta T}{\delta t}\right) = \{L\}^T([D]\{L\}T) + q_v \tag{13}$$

Where ρ, c, T, t, $\{L\}$, q_v, and $[D]$ are the density, specific heat, temperature, time, vector operator, internal heat generation, and conductivity matrix, respectively. The vector operator is expressed as shown in Eq 14.

$$\{L\} = \begin{Bmatrix} \frac{\partial}{\partial x} \\ \frac{\partial}{\partial y} \\ \frac{\partial}{\partial z} \end{Bmatrix}; [D] = \begin{bmatrix} k_{xx} & & \\ & k_{yy} & \\ & & k_{zz} \end{bmatrix} \tag{14}$$

Where k_{xx}, k_{yy}, and k_{zz} represent thermal conductivity in the x, y, and z directions, respectively. The determination of internal heat generation at every node, which is based on the Gaussian laser flux distribution, on which the subroutine code was based, is expressed in Eq 15.

$$q_{(x,y,z,t)} = \begin{cases} 0 & ; transparent\ part \\ (1 - R_a)KI_a \exp(-Kz_a)\,; & for\ the\ absorbent\ part \end{cases} \quad (15)$$

Where R_a, K, I_a, and z_a are the reflectivity of the absorbance, absorption coefficient of the absorbent part, laser intensity after passing through the transparent part, and the depth within the absorbent material, respectively. Eq 16 shows the full expression of laser intensity.

$$I_a = \frac{T_t P}{\pi r_0^2} exp\left(-\frac{r^2}{r_0^2}\right) \quad (16)$$

$$r = \sqrt{x_s^2} + y_s^2 \quad (17)$$

Where T_t, P, r_0, and r represent the transmissivity of the transparent polymer part, laser power, the laser beam radius, and radial distance of any point on the surface of the material, expressed in Eq 17, in which x_s and y_s represent the Cartesian coordinates at that point. This study considered temperature-dependent properties and heat losses due to convection and radiation. To account for the heat losses due to radiation and convection on the material surface to the surrounding, we imposed a combined convection-radiation boundary condition using Eq 18.

$$-k(T)\vec{\nabla}T\vec{n} = h_r(T_s - T_0) \quad (18)$$

Where h_r is the combined heat transfer coefficient, which is expressed as shown in Eq 19:

$$h_r = h + \varepsilon\sigma(T_s + T_0)(T_s^2 + T_0^2) \quad (19)$$

Where h and $\mathcal{E}$ are the convective heat transfer coefficient of polypropylene and emissivity of polypropylene, respectively. The emissivity of polypropylene in this study was 0.97, and the heat transfer coefficient (h) for the convective heat transfer part was considered as 10 W/(m^2·K) based on literature [16].

2.10. Material properties

In this study, the material properties considered for the LTW simulation in ABAQUS were density, thermal conductivity, and specific heat capacity. For the simulation of the LTW of PP containing 0.2% carbon black and 100% PP, the temperature-dependent function for specific heat capacity and thermal conductivity is shown in Table 4, which is taken from open literature. The optical properties (transmission, reflectance, and absorbance) for all the PP samples used in this study were determined experimentally using a NIR VIS spectrometer from Celeb Solutions for a wavelength of 987 nm. For oak wood fiber–reinforced PP, the thermal conductivity was determined using numerical methods, which was the effective thermal conductivity of the composite material from earlier sections. For the temperature-dependent specific heat capacity of the material, the TGA (DSC) experiments were utilized, and the material properties used were the ones determined from thermal characterization. The density of the composite materials was determined by the rule of matrix.

2.11. Numerical modeling of LTW

In this study, the FEA ABAQUS commercial software was used to conduct the FEM of a lap-joint configuration, as shown in Figure 8a. The 3D model has a finer mesh at the radiation zone of 0.025 mm, as shown in Figure 8b, and the rest of the model has a coarser mesh of 0.05 mm; the mesh type used was a C3D8 element type. A number of simulations were conducted to confirm the mesh density, increasing it until the calculated temperatures and temperature profiles were consistent. The summary of the mesh analysis is shown in Table 5, showing three configurations varying the weld zone mesh sizes (0.035, 0.025, and 0.015 mm). The weld irradiation zone mesh size of 0.025 mm was chosen after analyzing the trade-offs between computational efficiency and numerical accuracy. The findings show that 0.025 mm mesh size yields weld width and peak temperatures that are more in line with the finer mesh size of 0.015 mm, with a difference of less than 0.2%, showing convergence. The weld width for the mesh size of 0.025 mm is consistently greater than that attained with a coarser mesh size of 0.035 mm, suggesting that the weld shape has better spatial resolution for the mesh size of 0.025 mm. From a computational perspective, simulation with a 0.025 mm mesh size takes significantly less time than those with a mesh size of 0.015 mm, which maximizes resources without compromising the accuracy required for reliable analysis. Therefore, the 0.025 mm mesh size is justified as the optimum discretization level for this study since it offers an efficient compromise that guarantees sufficient resolution for weld width measurement and heat behavior while retaining reliable predictions.

Table 5. Effect of mesh size on weld width and peak temperature.

Configuration case	Weld zone mesh size (mm)	Simulation time (h)	Weld width (mm)	Peak temperature (K)
1	0.035	9	1.72	428.6
	0.025	12	1.85	449.9
	0.015	16	1.86	451.0
2	0.035	9	2.06	439.4
	0.025	12	2.17	451.1
	0.015	16	2.19	450.8
3	0.035	9	3.72	398.9
	0.025	12	4.00	455.2
	0.015	16	4.05	456.3

The Gaussian heat source for the internal heat generation was incorporated using the user subroutine coding in the FORTRAN programming language, which was based on the internal heat generation Gaussian expression in Eq 15. The Gaussian heat flux is applied to the body material on which the laser beam will be focused. The moving heat is created by using a subroutine in the FORTRAN language. The load position and magnitude are determined from the subroutine code and are computed to ensure convergence. The velocity of the heat flux is determined within the step module, the time step, which is based on welding velocity and the weld length. The subroutine code determines the heat flux's direction and position. The effect mimics a continuously moving laser beam. The transient heat transfer is then run, and the temperature width is documented to determine the weld

width. The simulation time for the 3D model was approximately 12 h using a Core i7-4790 CPU@3.60GH and 16 GB RAM.

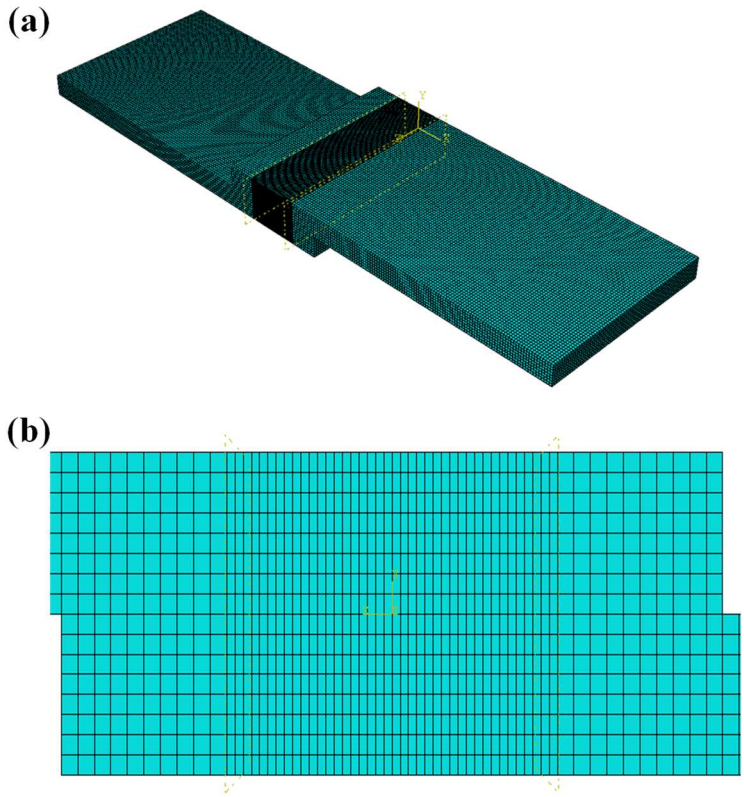

Figure 8. (a) Finite element 3D model mesh for LTW in lap-joint configuration with finer mesh in the weld zone. (b) Magnification of the finer mesh region.

To determine the laser transmission welding parameters shown in Table 6 to be used, multiple simulation runs were performed to identify parameter sets that produced consistent weld widths while minimizing the risk of material degradation. The range of parameters selected was based on prior experimental insights from the literature in laser transmission welding of polypropylene. For modeling, FEA plaques (70 × 35 × 4 mm) were used, which were joined in a lap-joint configuration with an overlap of 20 mm from the nearest edge. To simulate the laser contour welding of the sample, the laser beam was directed in the middle of the overlap, that is 10 mm from the nearest edge at the overlap of the transparent part (top part) and the absorbent part (bottom part), as shown in Figure 9.

Table 6. Laser-welding process parameters for polypropylene-based materials.

Case	Transparent part	Absorbent part	Laser power (W)	Welding speed (mm/min)	Laser beam diameter (mm)
1	100% polypropylene	Polypropylene with 0.2 wt% carbon black	21	400	1
2	100% polypropylene	Polypropylene with 0.2 wt% carbon black and 15 wt% oak wood fiber	21	400	1
3	Polypropylene containing 15 wt% oak wood fiber	Polypropylene with 0.2 wt% carbon black	33	175	1

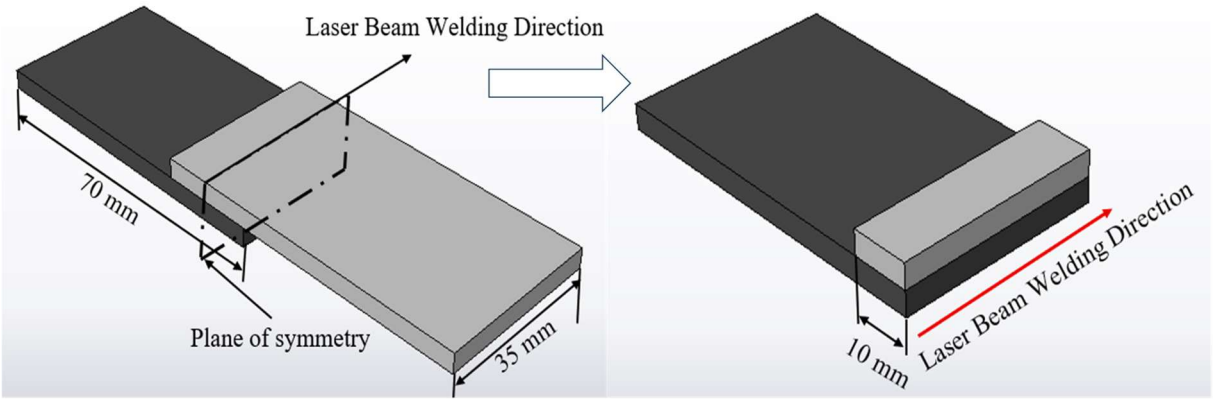

Figure 9. Schematic of the sample.

Figure 10 shows the temperature contour of welding parameters, which was done at parameters with a laser power of 21 W, welding speed of 400 mm/min, and a beam diameter of 1 mm for 100% PP as the transparent part and an absorbent part of PP containing 0.2 wt% CB. The average weld width was determined by measuring the width of the temperature contour representing the melt area, as shown in Figure 11. Figure 11 shows the temperature contour of welding parameters of laser power of 21 W, welding speed of 400 mm/min, and a beam diameter of 1 mm for 100% PP as the transparent part with PP containing 0.2% CB and 15% oak wood fiber by weight of the matrix material. From the results, the weld track width was determined by measuring the melt weld width from the temperature contours. Figure 12 shows the temperature contours of welding parameters at laser power of 33 W, welding speed of 175 mm/min, and laser beam diameter of 1 mm for joining PP containing 15% oak wood powder by weight of the polymer matrix as the top (transparent part) with PP containing 0.2% CB by weight of the polymer matrix as the bottom (absorbent) part. The average weld width was determined by measuring the width of the temperature contour representing the melt area, as shown in Figure 13.

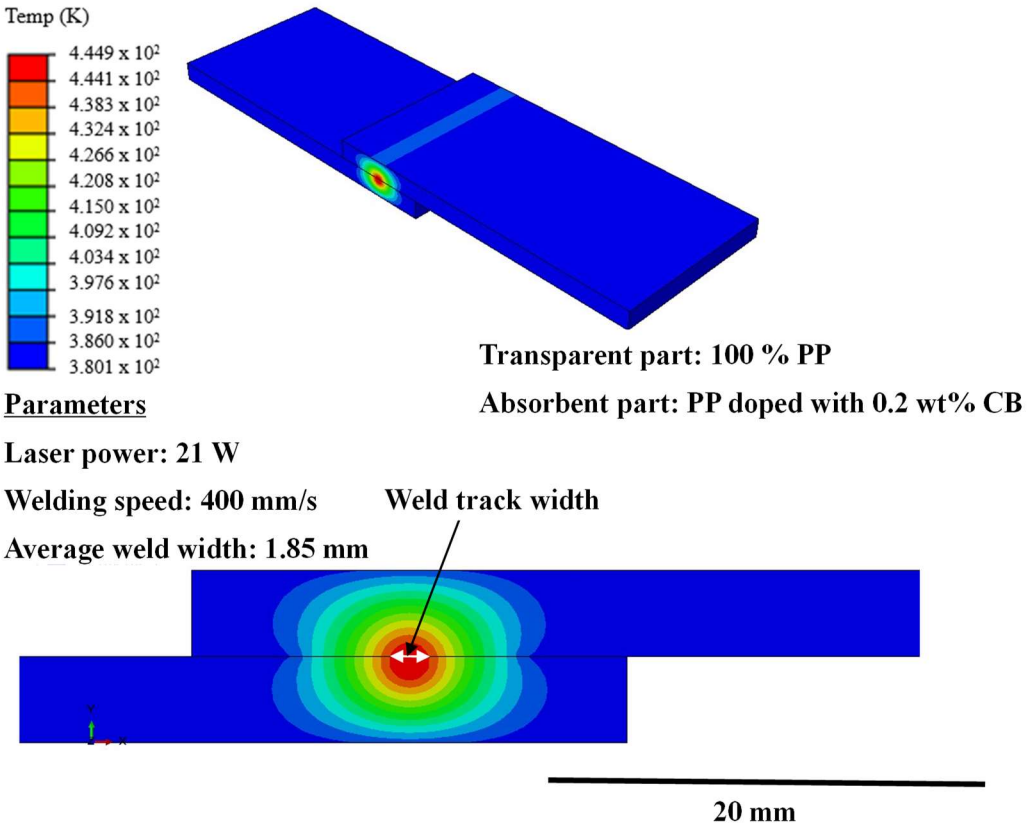

Figure 10. Laser transmission welding simulation results showing heat-distribution contours for case 1.

The cross-sectional view of the temperature distribution during the LTW of 100% PP as the transparent part and PP containing 0.2 wt% CB as the absorbent part is displayed in Figure 11, emphasizing the localized heating at the interface. The area of the weld seam width is the highest temperature concentration, known as the zone of effective thermal bonding, and is indicated by the welding track width. Kelvins (K) are the standard unit of measurement for temperature in ABAQUS software. By measuring the length at the interface, which represents the temperature range of 444.1–449.9 K, the weld track width is determined. For the weld size, the scale bar at the bottom provides a spatial reference of 20 mm. According to the TGA previously presented in this paper, the temperature range for joining the materials is within the melting range and does not surpass the degradation temperature, which represents the region of molecular fusion between the transparent and absorbent parts.

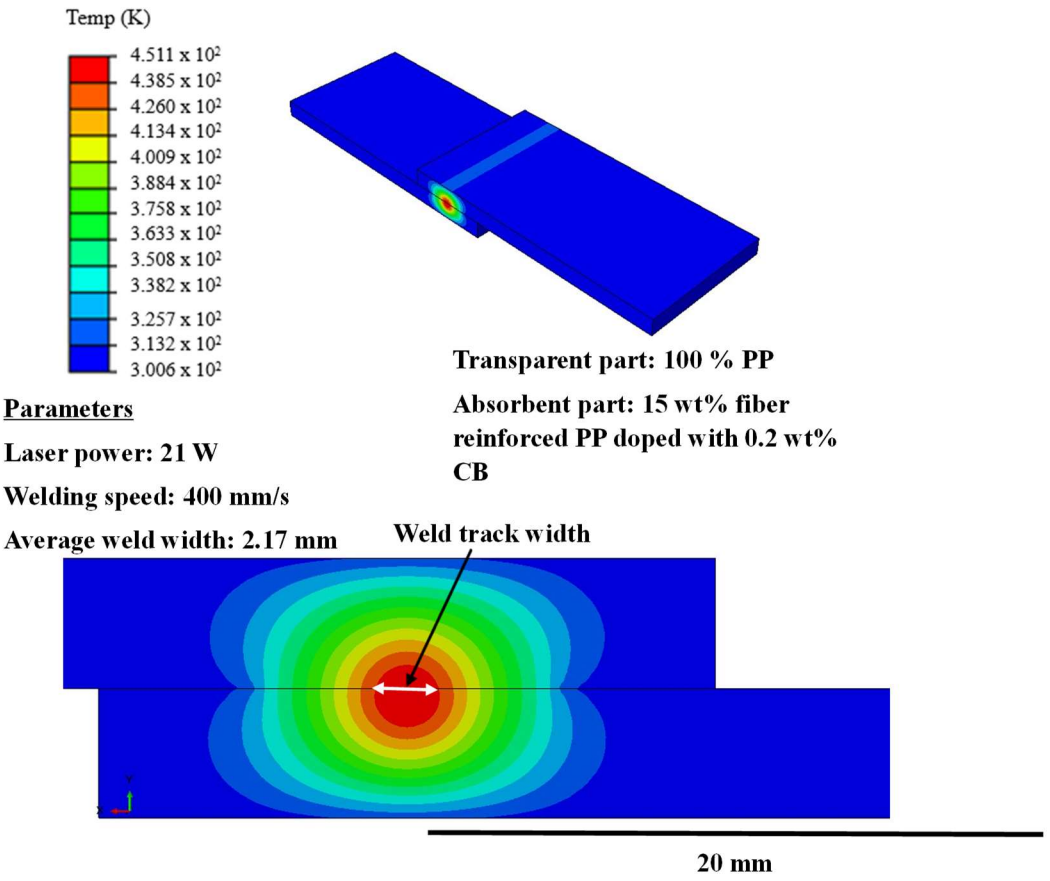

Figure 11. Laser transmission welding simulation results showing heat-distribution contours for case 2.

Localized heating at the interface is highlighted in the cross-sectional view of the temperature distribution during the LTW of 100% PP as the transparent part joined to an absorbent PP containing 0.2% CB and 15% oak wood fiber by weight of the matrix material in Figure 12. Located at the center of the weld seam, the zone of effective thermal bonding is indicated by the welding track width. In ABAQUS software, the temperature scales are automatically displayed in K. Based on the TGA previously presented in this paper, the weld track width is measured by measuring the length at the interface, representing the temperature range of 438.5–451.1 K. For the weld size, the scale bar at the bottom provides a spatial reference of 20 mm. The temperature range is within the melting range and does not exceed the degradation temperature, which represents the region of molecular fusion between the transparent part and the absorbent part.

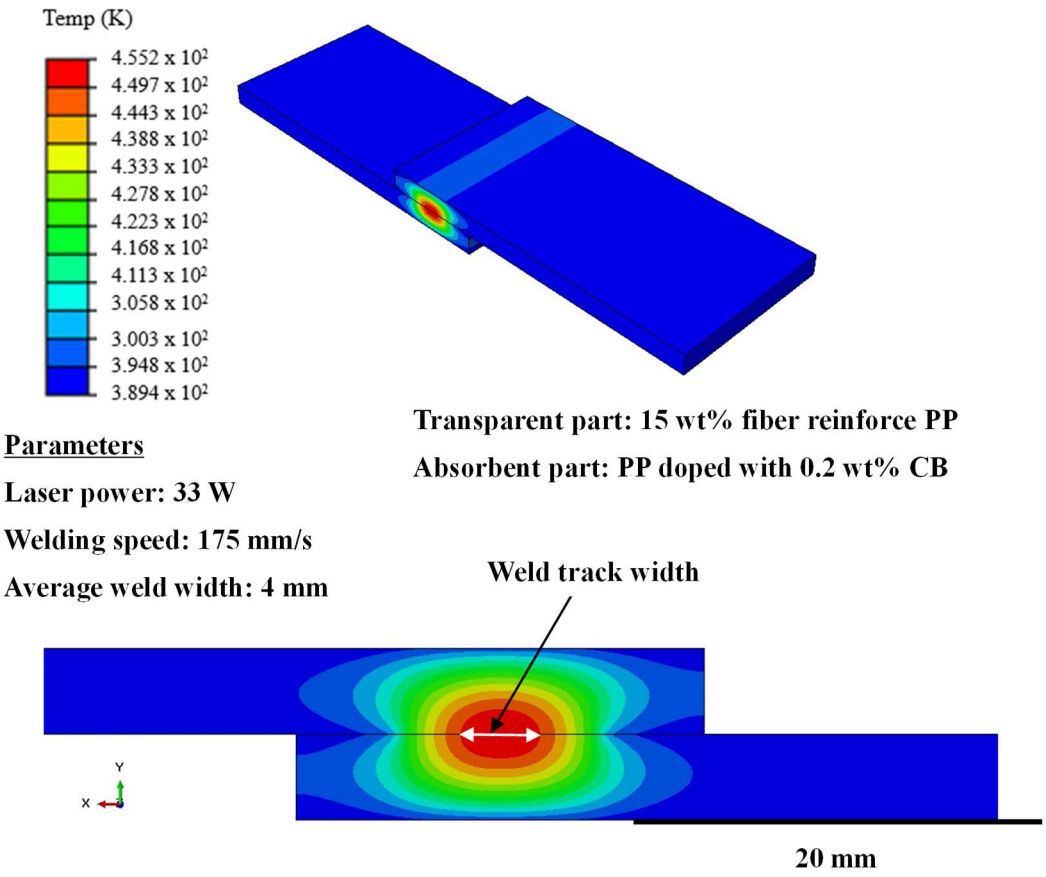

Figure 12. Laser transmission welding simulation results showing heat-distribution contours for case 3.

The temperature distribution during the LTW of PP containing 15% oak wood powder by weight of the polymer matrix as the top (transparent) part, joined to PP containing 0.2% CB by weight of the polymer matrix as the bottom (absorbent) part is shown cross-sectionally in Figure 13, emphasizing the confined heating at the interface. The zone of effective thermal bonding, or the highest temperature concentration in the middle of the weld seam, is displayed by the welding track width. By default, the ABAQUS program displays temperature scales in K. According to the TGA previously presented in this paper, the temperature range for joining the materials is within the melting range and does not exceed the degradation temperature, which represents the region of molecular fusion between the transparent part and the absorbent part. The weld track width is measured by measuring the length at the interface, which represents the temperature range of 449.7–455.2 K. The scale bar at the bottom gives the weld dimensions a spatial reference of 20 mm.

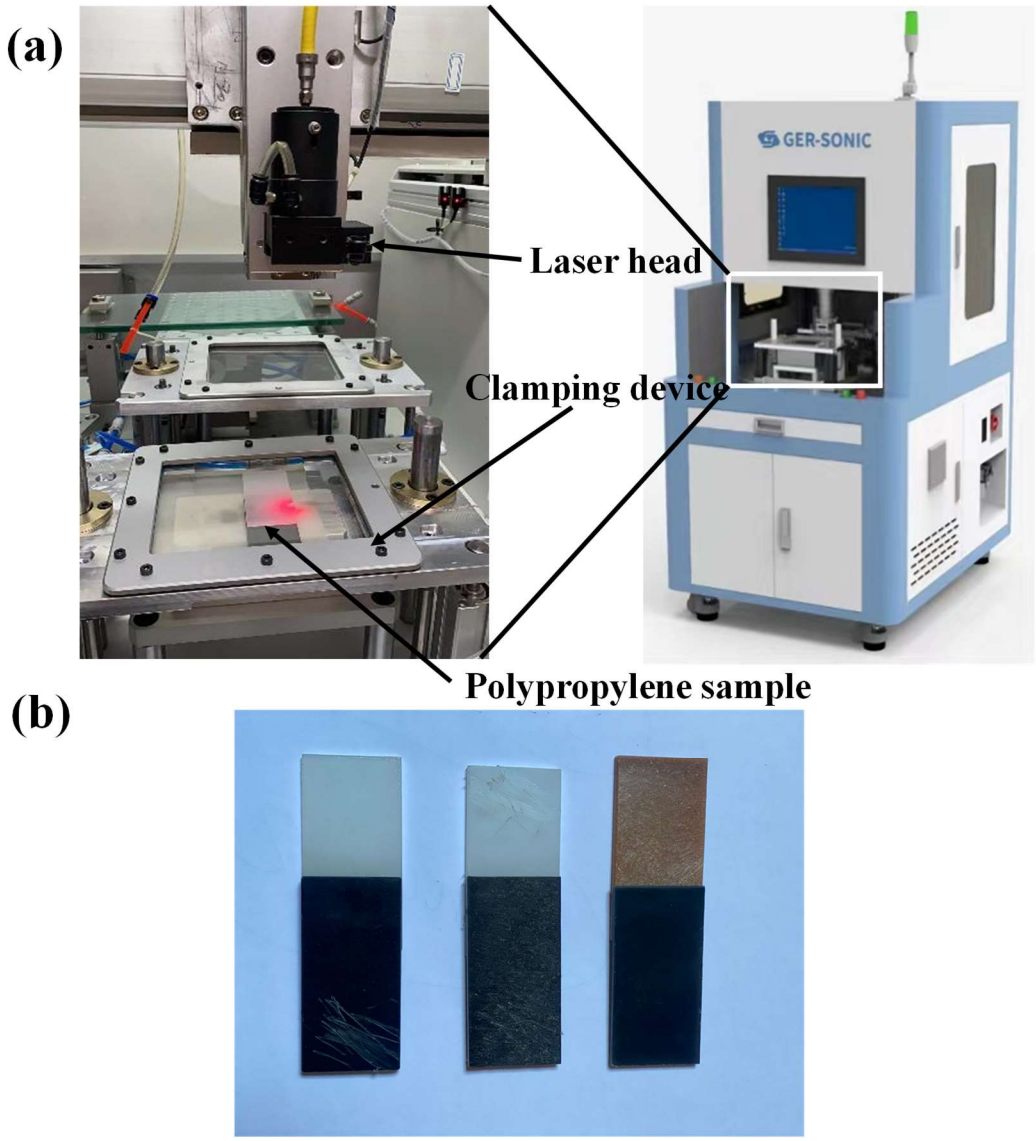

Figure 13. (a) Laser transmission welding experimental setup. (b) Samples joined using laser transmission welding.

2.12. Model validation

Experiments were conducted to validate the model for the LTW of the respective materials and simulated operating parameters. The experimental work was done using a Ger-sonic plastic welding machine model GS-3DLPW-300-35 equipped with a diode-semiconductor. The maximum optical power of the laser beam is 35 W, and the wavelength is 2000 nm. After conducting the LTW experimentally according to the operating parameters, an Instron H50KT Tinius Olsen universal testing machine was used to perform the lap shear pull test on the samples using a crosshead speed of 0.5 mm/min. To measure the weld track width, a Nikon microscope was used, as shown in Figure 14. The weld width was measured by taking the average of at least six measurements using Image J software. The experimental results were then compared with the modeling results.

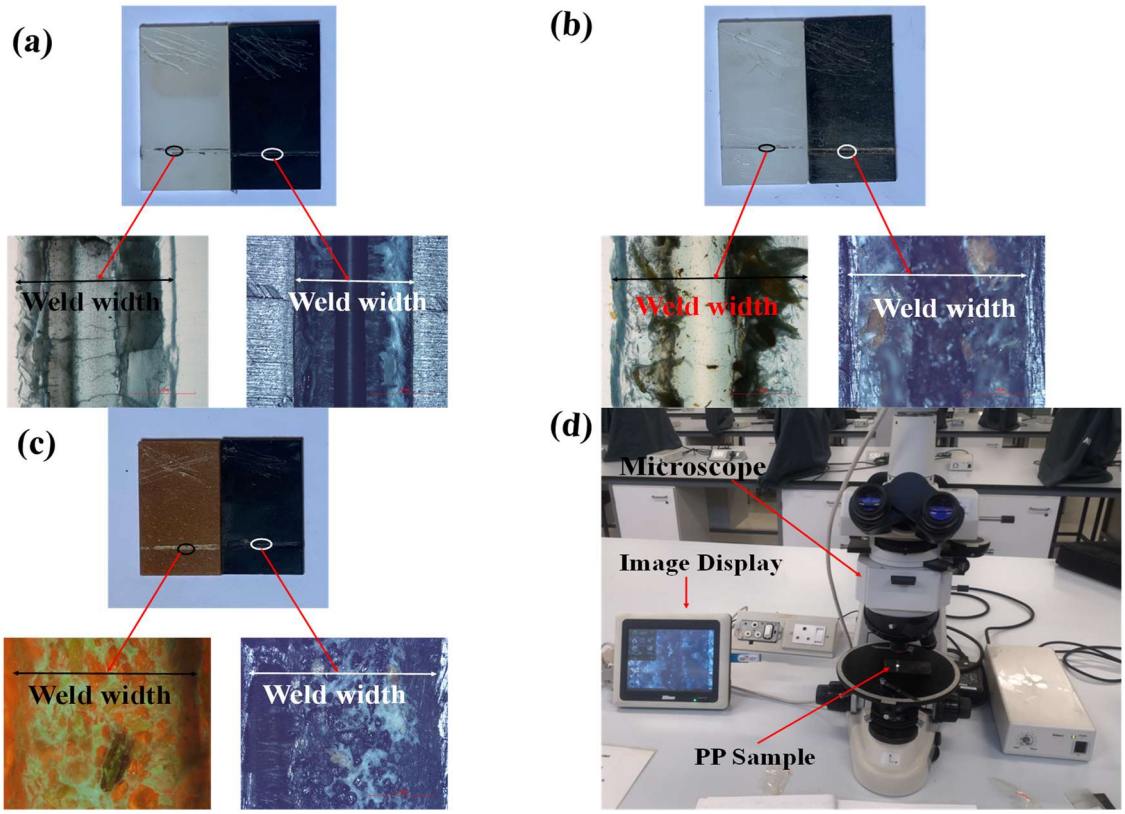

Figure 14. Weld width measurements using a microscope for the transparent and absorbent parts for (a) case 1, (b) case 2, and (c) case 3. (d) Experimental setup for measuring weld width using a microscope.

3. Results and discussion

Upon completion of the LTW experiments, the weld width from the simulations was compared with the weld width obtained experimentally by measuring the weld width on microscopic images, taking the average of at least three measurements.

Table 7. Comparison of simulation and experimental weld widths for samples without fiber reinforcement.

Run	Laser power (W)	Welding speed (mm/min)	Simulation weld width (mm)	Experimental weld width (mm)	Absolute error (%)
1	21	400	1.85	2.00	0.15
2	21	400	1.85	1.95	0.1
3	21	400	1.85	1.90	0.05
Root mean square error (RMSE)					0.108
Mean absolute error percentage (MAEP)					5.09

Table 7 shows a comparison of the weld width between the simulated results of the LTW of a 100% polypropylene transparent part joined to a polypropylene part doped with 0.2% CB absorbent

and the experimental results conducted under constant process parameters, with a laser power of 21 W and a welding speed of 400 mm/min. The experiments were repeated three times, and the results showed a high level of accuracy with an absolute error ranging from 0.05 to 0.15 mm. Quantitatively, from the three experiments conducted, the model achieved a RMSE of 0.108 and a MAEP of 5.09%, indicating that the simulation predicts an acceptable weld width.

Table 8. Comparison of simulation and experimental weld widths for samples with fiber reinforcement in the absorbent part.

Run	Laser power (W)	Welding speed (mm/min)	Simulation weld width (mm)	Experimental weld width (mm)	Absolute error (%)
1	21	400	2.17	2.01	0.16
2	21	400	2.17	2.00	0.17
3	21	400	2.17	1.99	0.18
RMSE					0.170
MAEP					8.5

Table 8 shows the comparison between experimental and simulated weld width results for a LTW of a 100% pure polypropylene transparent part joined to an absorbent polypropylene composed of 0.2 wt% carbon black and 15 wt% oak wood fiber. The comparison was conducted at a laser power of 21 W and a welding speed of 400 mm/min. The simulation results consistently overestimated the weld width, with errors ranging from 0.16 to 0.18 mm. The model accurately predicted the weld width with an RMSE of 0.0170 and an MAEP of 8.5%.

Table 9. Comparison of simulation and experimental weld widths for samples with fiber reinforcement in the transparent part.

Run	Laser power (W)	Welding speed (mm/min)	Simulation weld width (mm)	Experimental weld width (mm)	Absolute error (%)
1	33	175	400	4.10	0.10
2	33	175	400	4.09	0.09
3	33	175	400	4.08	0.08
RMSE					0.0904
MAEP					9

Table 9 shows a comparison of simulation and experimental weld width results for the LTW of a 15 wt% fiber-reinforced polypropylene transparent part joined to a 0.2 wt% carbon black–doped polypropylene absorbent part. The simulation and experiment were conducted at constant operating parameters, with a laser power of 33 W and a welding speed of 175 mm/min. The simulation results slightly underestimate the actual experimental results; however, the model predictions are acceptable, with an absolute error ranging from 0.08 to 0.10 mm, a RMSE of 0.0904, and a MAEP of 9%.

With regards to case 1, case 2, and case 3, there was a deviation of 7.5%, 8%, and 8.3%, respectively, of the simulated results from the experimental results, which was expected due to the inherent assumptions and simplifications of the simulation model. Discrepancies arise due to variations

in material properties, actual laser beam profile, and focal spot size, as well as measurement uncertainties, assumptions inherent in the modeling for determining the effective thermal conductivity of the composite material, and real-world variations such as non-uniform dispersion of the wood fibers and local changes in material density. When comparing case 1 and case 2, it is evident that the inclusion of natural fibers on the absorbent part increases the weld width, since the LTW input parameters were the same for case 1 and case 2. This is attributed to the effect of oak wood fibers on the thermal and optical properties of polypropylene. The presence of natural fibers in the absorbent part increases laser beam scattering and absorption, resulting in a wider weld width for identical laser transmission welding parameters, as they slightly increase the heat generated and retained in the weld region. Additionally, the presence of natural fibers reduced the effective thermal conductivity, thereby reducing heat dissipation compared to polypropylene in case 1, which lacks oak wood fiber reinforcement, allowing the melt zone to grow larger before solidification. Additionally, the presence of wood particles affects the local flow and wetting behavior within the molten material, thereby broadening the weld width. In case 3, the presence of natural fibers in the transparent part affects the transmittance of the incident laser beam, rendering the transparent part partially absorbent to the laser beam used in this study and scattering the laser beam. This results in increased laser power and a slower welding speed, ensuring that sufficient heat is generated at the weld interface to form a strong weld joint. Additionally, due to the greater energy density reaching the weld interface and the scattering of the laser beam by the transparent part, the weld joint was wider compared to cases 1 and 2, both lacking reinforcement in the transparent part.

4. Conclusions

This paper demonstrates how material characterization, effective thermal conductivity modeling, and transient heat transfer simulation offer a pathway to predict laser transmission weld joints of plant-based natural fiber–reinforced polypropylene. The FEA modeling and simulation were developed to determine the effect of plant-based fiber reinforcement on weld width in LTW of polypropylene, which was then validated experimentally. Three scenarios were considered. In the first scenario, 100% PP was used as the transparent part, while the absorbent part was PP containing 0.2 wt% CB. In the second scenario, 100% PP was used as the transparent part, and the absorbent part was PP containing 0.2 wt% CB and 15 wt% oak wood powder. In the third scenario, PP containing 15 wt% oak wood powder was used as the transparent part, and the absorbent part was PP containing 0.2 wt% CB in a lap joint configuration. Upon completion of the simulations, these were validated experimentally. The finite element framework in this paper reliably predicted the weld width of the oak wood fiber–reinforced polypropylene with minor deviations from the experimental measurements (less than 10%). When the oak wood fibers were introduced to either the transparent or absorbent parts, the weld seam width tended to widen due to more laser beam scattering and lower effective thermal conductivity. The TGA and TGA (DSC) results showed that 15 wt% oak wood fiber–reinforced polypropylene was thermally stable at temperatures at which the LTW of polypropylene is conducted. This enables safe LTW processing of composite materials without material degradation. The model demonstrated high predictive accuracy for the simulation of LTW without any fiber reinforcement, with an RMSE of 0.108 and a MAEP of 5.09%. This was followed by the model for predicting LTW of polypropylene with oak wood fiber reinforcement in the absorbent part, with an RMSE of 0.170 and a MAEP of 8.5%. In this case, the simulation slightly overestimated the weld width. Lastly, in the

simulation for the LTW of polypropylene with oak wood fiber-reinforced transparent part, the model slightly underestimated the weld width, with an RMSE of 0.904 and MAEP of 9%. Overall, the model proved capable of predicting reliable weld widths for different material configurations and process parameters. The highest accuracy was obtained when joining samples without oak wood fiber reinforcement. This drop in accuracy by the introduction of fibers was attributed to inconsistencies in material properties and further assumptions imposed on the model, both from the homogenization simulation to estimate effective thermal conductivity and the ROM estimation of the density of the composite material. To further improve the model used in this study, a more detailed optical characterization, which includes fiber dispersion, size distribution, and actual orientation, could be incorporated to reduce modeling assumptions, thereby improving the weld width predictions.

Use of AI tools declaration

The authors declare they have not used Artificial Intelligence (AI) tools in the creation of this article.

Author contributions

Munyaradzi Kapuyanyika performed the experiments, analysed the results, and wrote the manuscript. Albert Uchenna Ude and Vivekanandhan Chinnasamy provided supervision guidance and critical revisions of the manuscript.

Conflict of interest

The authors declare no conflict of interest.

References

1. Jabeen R, Cosson B, Akué AA, et al. (2023) Effect of fibre orientation on the light scattering during laser transmission welding. *J Manuf Process* 86: 1–9. https://doi.org/10.1016/j.jmapro.2022.12.042
2. Ramesh M, Nijanthan S (2016) Mechanical property analysis of kenaf–glass fibre reinforced polymer composites using finite element analysis. *Bull Mater Sci* 39: 147–157. https://doi.org/10.1007/s12034-015-1129-z
3. Goyal DK, Yadav R, Kant R, et al. (2022) An integrated hybrid methodology for estimation of absorptivity and interface temperature in laser transmission welding. *Int J Adv Manuf Tech* 121: 3771–3786. https://doi.org/10.1007/s00170-022-09536-y
4. Fernandes FAO, Pereira AB, Guimarães B, et al. (2020) Laser welding of transmitting high-performance engineering thermoplastics. *Polymers* 12: 402. https://doi.org/10.3390/polym12020402
5. Acherjee B (2019) FEM-ANN sequential modelling of laser transmission welding for prediction of weld pool dimensions, In: Kumar K, Kumari N, Davim J, *Non-Conventional Machining in Modern Manufacturing Systems*, Hershey, PA: IGI Global Scientific Publishing, 249–261. https://doi.org/10.4018/978-1-5225-6161-3.ch012

6. Acherjee B, Kuar AS, Mitra S, et al. (2013) Finite element simulation of laser transmission thermoplastic welding of circular contour using a moving heat source. *IJMMS* 6: 437–454. http://dx.doi.org/10.1504/IJMMS.2013.058522
7. Hu S, Li F, Zuo P, et al. (2023) Numerical simulation of laser transmission welding—A review on temperature field, stress field, melt flow field, and thermal degradation. *Polymers* 15: 2125. https://doi.org/10.3390/polym15092125
8. Deng K, Nejadkhaki HK, Pasquali FM, et al. (2019) Rule of mixtures model to determine elastic modulus and tensile strength of 3D printed carbon fiber reinforced nylon. Proceedings of the ASME 2019 International Design Engineering Technical Conferences and Computers and Information in Engineering Conference. Volume 2A: 45th Design Automation Conference. Anaheim, California, USA. August 18–21, 2019. V02AT03A039. ASME. https://doi.org/10.1115/DETC2019-98024
9. Nguyen PQ, Zohdi N, Zhang YX, et al. (2024) Study on material behaviours of additively manufactured high-impact polystyrene using artificial neural networks. *Prog Addit Manuf* 10: 1461–1478. https://doi.org/10.1007/s40964-024-00718-6
10. Yerbolat G, Amangeldi S, Ali MH, et al. (2018) Composite materials property determination by rule of mixture and Monte Carlo simulation. Proceedings of the 2018 IEEE International Conference on Advanced Manufacturing, ICAM 2018, 1, 384–387. https://doi.org/10.1109/AMCON.2018.8615034
11. Akué Asséko AC, Cosson B, Deleglise M, et al. (2015) Analytical and numerical modeling of light scattering in composite transmission laser welding process. *Int J Mater Form* 8: 127–135. https://doi.org/10.1007/s12289-013-1154-7
12. Xu W, Li P, Liu H, et al. (2022) Numerical simulation of molten pool formation during laser transmission welding between PET and SUS304. *Int Commun Heat Mass Transfer* 131: 105860. https://doi.org/10.1016/j.icheatmasstransfer.2021.105860
13. Wang C, Liu H, Chen Z, et al. (2021) A new finite element model accounting for thermal contact conductance in laser transmission welding of thermoplastics. *Infrared Phys Technol* 112: 103598. https://doi.org/10.1016/j.infrared.2020.103598
14. Chen Z, Zhou H, Wu C, et al. (2022) A cleaner production method for laser transmission welding of two transparent PMMA parts using multi-core copper wire. *J Mater Res Technol* 16: 1–12. https://doi.org/10.1016/j.jmrt.2021.11.157
15. Acherjee B, Kuar AS, Mitra S, et al. (2012) Modeling of laser transmission contour welding process using FEA and DoE. *Opt Laser Technol* 44: 1281–1289. https://doi.org/10.1016/j.optlastec.2011.12.049
16. Ali MM, Dave F, Sherlock R, et al. (2021) Simulated effect of carbon black on high speed laser transmission welding of polypropylene with low line energy. *Front Mater* 8: 1–14. https://doi.org/10.3389/fmats.2021.737689
17. Anh-Duc L, Cosson B, Akué Asséko AC, et al. (2023) Investigation of the effect of light scattering on transmitted laser intensity at the weld interface during laser transmission welding of 3D printed thermoplastic parts. *Int J Mater Form* 16: 65. https://doi.org/10.1007/s12289-023-01786-9
18. Acherjee B (2021) Laser transmission welding of dissimilar plastics: 3-D FE modeling and experimental validation. *Weld World* 65: 1429–1440. https://doi.org/10.1007/s40194-021-01079-2

19. Long Q, Qiao H, Yu X, et al. (2022) Modeling and experiments of the thermal degradation behavior of PMMA during laser transmission welding process. *Int J Heat Mass Tran* 194: 123086. https://doi.org/10.1016/j.ijheatmasstransfer.2022.123086
20. Kumar D, Sarkar NS, Acherjee B, et al. (2022) Beam wobbling effects on laser transmission welding of dissimilar polymers: Experiments, modeling, and process optimization. *Opt Laser Technol* 146: 107603. https://doi.org/10.1016/j.optlastec.2021.107603
21. Sankara H, Baillis D, Coulibaly O, et al. (2024) Computational model of effective thermal conductivity of green insulating fibrous media. *Materials* 17: 252. https://doi.org/10.3390/ma17010252
22. Chen Z, Huang Y, Han F, et al. (2018) Numerical and experimental investigation on laser transmission welding of fiberglass-doped PP and ABS. *J Manuf Process* 31: 1–8. https://doi.org/10.1016/j.jmapro.2017.10.013
23. Lagüela S, Bison P, Peron F, et al. (2015) Thermal conductivity measurements on wood materials with transient plane source technique. *Thermochim Acta* 600: 45–51. https://doi.org/10.1016/j.tca.2014.11.021

AIMS Press